NUMERICAL INVESTIGATION OF STRONGLY NON-LINEAR TRANSONIC FLOW PROBLEMS AROUND THE AIRFOIL

Satoru Yamamoto*

Tohoku University
Sendai 980-77, Japan

Abstract

The purpose of the present paper is first to propose a higher-resolution numerical method for simulating unsteady transonic viscous flows around the airfoil considering the gas-liquid phase change which must be one of typical non-linear flow problems, and next the complicated flow phenomena also involving shocks, vortices and their interactions are preliminary investigated. The fundamental equations composed of the compressible Navier-Stokes equations and the model equations for the phase change based on the classical condensation theory are solved using the fourth-order accurate compact MUSCL TVD scheme and the maximum second-order implicit scheme proposed by the author. As numerical examples, steady and unsteady transonic viscous flows around the NACA0012 airfoil in the moist air at low and high angles of attack are calculated and the results are compared to that in dry air. Then, the phase change and the induced condensation shock are clearly obtained. Finally the influence of the humidity to the airfoil performance is numerically estimated.

1. Introduction

A lot of 3D compressible Navier-Stokes solvers has been already developed in order to investigate the performance of the airfoil.[1,2] However, non-linear flow problems in the aeronautics, for examples, strongly unsteady flows may have never been accurately investigated yet. The unsteady flows should be calculated using a higher-order accurate numerical method in both space discretization and time integration.

Transonic viscous flows around the airfoil have been already calculated assuming a steady state solution.[3,4] Accurate results which have been very consistent with the experiment have being obtained using novel high-resolution numerical methods.[5,6] Of course, unsteady 3D flows around the complicated configuration at high angle of attack also have been numerically investigated, for examples, in Refs.7 and 8. However, most of them have been limited at the subsonic speed. It seems that unsteady flow problems at the transonic speed around the airfoil at high angle of attack still have been too difficult for the existing numerical method to solve accurately. It is known that not only a normal shock but a large separation of the boundary layer are observed in the transonic viscous flow at the high angle. The shock itself may be highly resolved using a high-resolution shock capturing method[6] which has second-order accuracy in space, whereas it seems that vortices which are induced from the interaction between the shock and the boundary layer separation should be calculated using a higher-order accurate method both in space discretization and time integration. Since most of the shock capturing method have at most second-order accuracy in space, vortices could not always be resolved clearly.

Recently we have proposed a higher-resolution numerical method[9] composed of the fourth-order accurate compact MUSCL TVD scheme in space and the maximum second-order accurate implicit approximate-factorization scheme in time. The numerical results when unsteady transonic viscous flows around a cylinder have been calculated using the method have suggested that a higher-order accurate scheme both in space and time must have been used for simulating a flow problem involving strongly unsteadiness such as the interaction between the strong shock and the large separated boundary layer.[10]

As another strongly non-linear flow problem, the gas-liquid two-phase flow around the airfoil must be pointed out, for examples, the flight in the moist air or bad atmosphere. The two-phase flow should be calculated using model equations for the condensation and the phase change as well as using the higher-resolution method. The numerical investigations of transonic gas-liquid two-phase flows have been already reported in recent papers.[11-13] Young[11] has calculated the wet steam flow through the final stage turbine channel. Schnerr et al.[12] has investigated the transonic inviscid

*Associate Professor, Dept. of Aeronautics and Space Engineering, Member AIAA, JSASS

Copyright © 1996 by the AIAA and ICAS. All rights reserved.

flow around the airfoil in the moist air. Ishizaka et al.[13] has proposed a higher-resolution numerical method for investigating the transonic flow through the wet steam turbine channel.

The purpose of this paper is first to extend the numerical method proposed by Ishizaka et al. into the method for simulating steady transonic viscous flows around the airfoil at low angle of attack in the moist air considering the humidity, and next the method is applied to the CFD code developed in Ref.10 for simulating unsteady transonic viscous flows around the airfoil at high angle of attack also considering the humidity. Finally, the flow characteristics around the airfoil associated with the moist air is numerically explained and the influence to the airfoil performance is preliminary estimated.

2. Fundamental Equations

The fundamental equations are composed of the 2D compressible Navier-Stokes equations and the mass conservation equations of the vapor, the liquid, and the number density of droplet, in general curvilinear coordinates. The homogeneous multiphase fluid without the velocity slip is assumed.

$$\partial\hat{Q}/\partial t + \hat{\mathcal{F}}(\hat{Q}) = \frac{\partial \hat{Q}}{\partial t} + \frac{\partial \hat{F}_i}{\partial \xi_i} + \hat{S} + \hat{H} = 0 \tag{1}$$

where

$$\hat{Q} = J\begin{bmatrix} \rho \\ \rho u_1 \\ \rho u_2 \\ e \\ \rho_v \\ \rho\beta \\ \rho n \end{bmatrix}, \quad \hat{F}_i = J\begin{bmatrix} \rho U_i \\ \rho u_1 U_i + \partial\xi_i/\partial x_1 p \\ \rho u_2 U_i + \partial\xi_i/\partial x_2 p \\ (e+p)U_i \\ \rho_v U_i \\ \rho\beta U_i \\ \rho n U_i \end{bmatrix}$$

$$\hat{S} = -J\frac{\partial\xi_i}{\partial x_j}\frac{\partial}{\partial\xi_i}\begin{bmatrix} 0 \\ \tau_{1j} \\ \tau_{2j} \\ \tau_{kj}u_k + (\kappa+\kappa^t)\partial T/\partial x_j \\ 0 \\ 0 \\ 0 \end{bmatrix}$$

$$\hat{H} = -J\begin{bmatrix} 0 \\ 0 \\ 0 \\ 0 \\ -\Gamma \\ \Gamma \\ \rho I \end{bmatrix}$$

t, x_i, ξ_i, ρ, u_i, and e are the time, cartesian coordinates, general curvilinear coordinates, density, cartesian components of the physical velocity, and the total internal energy per unit volume, respectively. U_i, T, κ, κ^t, and J are the components of the contravariant velocity, temperature, heat conductivity, eddy heat diffusivity, and the Jacobian, respectively. ρ_v, β, n, Γ, and I are the density of vapor, mass fraction of liquid phase, number density of droplet, mass generation rate due to the condensation, and the homogeneous nucleation rate, respectively. τ_{ij} of the stress tensor Π are defined as

$$\tau_{ij} = (\mu+\mu_t)[(\frac{\partial u_i}{\partial x_j} + \frac{\partial u_j}{\partial x_i}) - \frac{2}{3}\delta_{ij}\frac{\partial u_k}{\partial x_k}]$$

where μ, μ_t and δ_{ij} are the molecular viscosity, eddy viscosity and the Krónecker delta, respectively. The molecular viscosity μ is derived from the linear combination between that of the gas phase and that of the liquid phase using the mass fraction β. The eddy viscosity is preliminary evaluated from a modified Baldwin-Lomax turbulence model[14].

The equation of state and the speed of sound, which have been already derived in Ref.13, are written as

$$p = \rho RT(1-\beta) \tag{2}$$

$$c = [\frac{C_{pm}}{C_{pm}-(1-\beta)R}\frac{p}{\rho}]^{1/2} \tag{3}$$

where

$$R = (\frac{\rho_a R_u}{\rho_g M_a} + \frac{\rho_v R_u}{\rho_g M_v})$$

ρ_a and M_a are the density of dry air and its mass per molecule, and also ρ_g and M_g are those of gas phase. R_u is the universal gas constant. C_{pm} is defined as the linear combination of the specific heat at constant pressure between the gas phase and the liquid phase using the mass fraction β.

The mass generation rate Γ considering the non-equilibrium condensation is approximated using the classical condensation theory. It is decided from the sum of the homogeneous nucleation and the mass increment according to the growth of the droplet as

$$\Gamma = \frac{4}{3}\pi\rho_\ell I r_*^3 + 4\pi\rho_\ell \sum n_i r_i^2 \frac{dr_i}{dt} \tag{4}$$

r and r_* are the droplet radius and the critical droplet radius by Kelvin-Helmholtz, respectively. The nucleation rate I is referred from Ref.15 and the surface tension is evaluated from Ref.16. The growth of the droplet is calculated from the Hertz-Knudsen model[17].

3. Space Discretization

3.1 Fourth-order compact MUSCL TVD scheme

One of the present numerical scheme for space discretization of $\hat{F}_i$ is the fourth-order accurate

compact MUSCL TVD scheme[9]. The 1D scalar conservation law is used to explain the scheme briefly, that is,

$$\frac{\partial u}{\partial t} + \frac{\partial f}{\partial x} = 0 \tag{5}$$

Then, the semi-discrete form of Eq.(5) can be written as

$$\frac{\partial u}{\partial t} + \frac{1}{\Delta x}(\hat{f}_{\ell+1/2} - \hat{f}_{\ell-1/2}) = 0 \tag{6}$$

ℓ is a discretized point along x. The numerical function $\hat{f}_{\ell+1/2}$ can be written in MUSCL form as

$$\hat{f}_{\ell+1/2} = f^+(u^L_{\ell+1/2}) + f^-(u^R_{\ell+1/2}) \tag{7}$$

The unknown functions u^L, u^R are generally extrapolated using the MUSCL approach[18].

On the other hand, the flux function of the fourth (fifth)-order accurate MUSCL scheme[9] can be written as

$$\begin{aligned}\hat{f}_{\ell+1/2} &= f^+(u^L_{\ell+1/2} + \Delta^3 u^{L(4)}_{\ell+1/2}) \\ &+ f^-(u^R_{\ell+1/2} + \Delta^3 u^{R(4)}_{\ell+1/2})\end{aligned} \tag{8}$$

where

$u^L_{\ell+1/2} = u_\ell + \frac{1}{6}(\Delta u_{\ell-1/2} + 2\Delta u_{\ell+1/2})$

$u^R_{\ell+1/2} = u_{\ell+1} - \frac{1}{6}(2\Delta u_{\ell+1/2} + \Delta u_{\ell+3/2})$

$\Delta^3 u^{L(4)}_{\ell+1/2} = -\frac{1}{6}(\frac{1-\phi}{4}\Delta^3 u_{\ell-1/2} + \frac{1+\phi}{4}\Delta^3 u_{\ell+1/2})$

$\Delta^3 u^{R(4)}_{\ell+1/2} = \frac{1}{6}(\frac{1+\phi}{4}\Delta^3 u_{\ell+1/2} + \frac{1-\phi}{4}\Delta^3 u_{\ell+3/2})$

$\Delta u_{j+1/2} = u_{j+1} - u_j$

$\Delta^3 u_{j+1/2} = \Delta u_{j-1/2} - 2\Delta u_{j+1/2} + \Delta u_{j+3/2}$

This scheme becomes fifth-order accuracy only for $\phi = 1/5$. The present fourth-order accurate compact MUSCL TVD scheme is introduced by $\phi = 1/3$.

$$\hat{f}_{\ell+1/2} = f^+(u^L_{\ell+1/2}) + f^-(u^R_{\ell+1/2}) \tag{9}$$

where

$u^L_{\ell+1/2} = u_\ell + \frac{1}{6}(\Delta^* \bar{u}_{\ell-1/2} + 2\Delta^* \tilde{u}_{\ell+1/2})$

$u^R_{\ell+1/2} = u_{\ell+1} - \frac{1}{6}(2\Delta^* \bar{u}_{\ell+1/2} + \Delta^* \tilde{u}_{\ell+3/2})$

$\Delta^* \tilde{u}_{j+1/2} = \mathrm{m}(\Delta^* u_{j+1/2},\ b_1 \Delta^* u_{j-1/2})$

$\Delta^* \bar{u}_{j+1/2} = \mathrm{m}(\Delta^* u_{j+1/2},\ b_1 \Delta^* u_{j+3/2})$

$\Delta^* u_{j+1/2} = \Delta u_{j+1/2} - \frac{1}{6}\Delta^3 \bar{u}_{j+1/2}$

$\Delta^3 \bar{u}_{j+1/2} = \Delta \bar{u}_{j-1/2} - 2\Delta \bar{u}_{j+1/2} + \Delta \bar{u}_{j+3/2}$

$\Delta \bar{u}_{j-1/2} = \mathrm{m}(\Delta u_{j-1/2},\ b_2 \Delta u_{j+1/2},\ b_2 \Delta u_{j+3/2})$

$\Delta \bar{u}_{j+1/2} = \mathrm{m}(\Delta u_{j+1/2},\ b_2 \Delta u_{j+3/2},\ b_2 \Delta u_{j-1/2})$

$\Delta \bar{u}_{j+3/2} = \mathrm{m}(\Delta u_{j+3/2},\ b_2 \Delta u_{j-1/2},\ b_2 \Delta u_{j+1/2})$

$\mathrm{m}(x, y, z) = s \cdot \max[0, \min\{|\ x\ |, s \cdot y, s \cdot z\}]$

$s = \mathrm{sign}(x)$

As the above expression, since the present scheme could be derived as a very compact formulation in which the basic form is completely same with the ordinary third-order MUSCL TVD scheme, the following advantages can be remarked. i) the monotone property and the TVD condition are completely satisfied using the two-step limiter functions. ii) the algorithm is very simple compared to the existing high-resolution scheme such as the ENO scheme[19]. iii) a new code based on the present scheme can be easily made if it is extended from the MUSCL-based code.

3.2 Flux Vector Splitting(FVS)

Equation (7) is extended to the system of equations and the numerical flux composed of the linearized flux-vector terms is defined as

$$\begin{aligned}(\hat{F}_i)_{\ell+1/2} &= (A_i^+)_{\ell+1/2}\hat{Q}^L_{\ell+1/2} \\ &+ (A_i^-)_{\ell+1/2}\hat{Q}^R_{\ell+1/2}\end{aligned} \tag{10}$$

$A_i^\pm (i = 1, 2)$ are the Jacobian matrices composed of only positive or negative eigenvalues, respectively. $\hat{Q}^{L(R)}$ is the vector of the extrapolated unknown variables, which are calculated using the fourth-order compact MUSCL TVD scheme. Finally, $(\hat{A}_i^\pm)_{\ell+1/2}\hat{Q}^M$, in which M is $L(R)$ if $A = A^{+(-)}$, can be written in the vector form composed of sub-vectors as

$$\begin{aligned}&(\hat{A}_i^\pm)_{\ell+1/2}\hat{Q}^M \\ &= \bar{\lambda}_{i1}^\pm \hat{Q}^M + \frac{\bar{\lambda}_{ia}^\pm}{\bar{c}\sqrt{g_{ii}}}\bar{Q}_{ia} + \frac{\bar{\lambda}_{ib}^\pm}{\bar{c}^2}\bar{Q}_{ib}\end{aligned} \tag{11}$$

where

$\lambda_{i1} = U_i,\ \lambda_{i4} = U_i + c\sqrt{g_{ii}},\ \lambda_{i5} = U_i - c\sqrt{g_{ii}}$

$\lambda_{ia}^\pm = \frac{1}{2}(\lambda_{i4}^\pm - \lambda_{i5}^\pm),\ \lambda_{ib}^\pm = \frac{1}{2}(\lambda_{i4}^\pm + \lambda_{i5}^\pm) - \lambda_{i1}^\pm$

$\bar{Q}_{ia} = \bar{p}\bar{Q}_{ic} + \Delta\bar{m}_i\bar{Q}_d,\ \bar{Q}_{ib} = \Delta\bar{m}_i\bar{Q}_{ic} + \bar{p}\bar{Q}_d$

$\bar{p} = \bar{Q}_p \cdot \hat{Q}^M,\ \Delta\bar{m}_i = \bar{Q}_{im} \cdot \hat{Q}^M$

$$Q_{ic} = \begin{bmatrix} 0 \\ \partial\xi_i/\partial x_1 \\ \partial\xi_i/\partial x_2 \\ U_i \\ 0 \\ 0 \\ 0 \end{bmatrix},\quad Q_d = \begin{bmatrix} 1 \\ u_1 \\ u_2 \\ (e+p)/\rho \\ \rho_v/\rho \\ \beta \\ n \end{bmatrix}$$

$$Q_p = \begin{bmatrix} \phi^2 \\ -\tilde{\gamma}u_1 \\ -\tilde{\gamma}u_2 \\ \tilde{\gamma} \\ 0 \\ 0 \\ 0 \end{bmatrix},\quad Q_{im} = \begin{bmatrix} -U_i \\ \partial\xi_i/\partial x_1 \\ \partial\xi_i/\partial x_2 \\ 0 \\ 0 \\ 0 \\ 0 \end{bmatrix}$$

Eq.(11) is linearized more exactly than the original Steger-Warming(S-W) FVS[20] to consider the Riemann problem. Therefore, one of the weak

points for the S-W FVS which it is inaccurate in the boundary layer region, can be overcome completely by introducing the averaging of sonic points as the overlined variables.

3.3 Flux Difference Splitting(FDS)

Another approximate Riemann solver based on the Roe's FDS[21] also can be introduced. The numerical flux $(\hat{F}_i)_{\ell+1/2}$ is written as

$$\begin{aligned}(\hat{F}_i)_{\ell+1/2} &= \frac{1}{2}[\hat{F}_i(\hat{Q}^L_{\ell+1/2}) + \hat{F}_i(\hat{Q}^R_{\ell+1/2}) \\ &- |(\hat{A}_i)_{\ell+1/2}|(\hat{Q}^R_{\ell+1/2} - \hat{Q}^L_{\ell+1/2})]\end{aligned} \quad (12)$$

$(\hat{A}_i)_{\ell+1/2}(i = 1,2)$ are evaluated from the Roe's averaging and

$$\begin{aligned}|(\hat{A}_i)|_{\ell+1/2}\hat{Q}^M &= |\bar{\lambda}_{i1}|\hat{Q}^M + \frac{|\bar{\lambda}_{ia}|}{\bar{c}\sqrt{g_{ii}}}\bar{Q}_{ia} \\ &+ \frac{|\bar{\lambda}_{ib}|}{\bar{c}^2}\bar{Q}_{ib}\end{aligned} \quad (13)$$

where

$$\begin{aligned}|\lambda_{ia}| &= \frac{1}{2}(|\lambda_{i4}| - |\lambda_{i5}|) \\ |\lambda_{ib}| &= \frac{1}{2}(|\lambda_{i4}| + |\lambda_{i5})|) - |\lambda_{i1}|\end{aligned}$$

Actually, both the FVS form Eq.(11) and the FDS form Eq.(12) have almost similar property, because the FVS form Eq.(11) is originally derived from the Roe's FDS.

4. Time Integration

4.1 Steady Calculation

The fundamental equations Eq.(1) are numerically integrated using the implicit time-marching method discretized by the delta-form approximate factorization, the diagonalization and the upstreaming for the steady state solution. Then, the following steps are executed

$$\begin{aligned}&\text{Step 1} \quad [I + \theta\Delta t(\Lambda_1^+\nabla_1 + \Lambda_1^-\Delta_1)]\Delta\hat{Q}^* \\ &\qquad = -\Delta t\hat{L}_1 N \cdot RHS^n \\ &\text{Step 2} \quad [I + \theta\Delta t(\Lambda_2^+\nabla_2 + \Lambda_2^-\Delta_2)]\Delta\hat{Q}^n \\ &\qquad = \hat{L}_2\hat{L}_1^{-1}\Delta\hat{Q}^* \\ &\text{Step 3} \quad \Delta\hat{Q}^n = N^{-1}\hat{L}_2^{-1}\Delta\hat{Q}^n\end{aligned} \quad (14)$$

where

$$RHS^n = -\Delta t\hat{\mathcal{F}}^*(\hat{Q})$$

$\theta = 1/2$ or 1, ∇_i and Δ_i are the backward- and forward-difference operators, respectively. $\hat{\mathcal{F}}^*$ is defined as the difference operators of $\hat{\mathcal{F}}$. $\hat{L}_i(i = 1,2)$ are the matrices composed of left eigenvectors in the nonconservative form, and N is a matrix for the transformation from the conservative form to the nonconservative form.

4.2 Unsteady Calculation

Eq.(14) is modified to a maximum second-order implicit method by introducing the Newton iteration and the Crank-Nicholson method. Finally, Eq.(14) is rewritten as

$$\begin{aligned}&\text{Step 1} \quad [I + \theta\Delta t(\Lambda_1^+\nabla_1 + \Lambda_1^-\Delta_1)]^m\Delta\hat{Q}^{*m} \\ &\qquad = -\Delta t(\hat{L}_1 N)^m \cdot RHS^m \\ &\text{Step 2} \quad [I + \theta\Delta t(\Lambda_2^+\nabla_2 + \Lambda_2^-\Delta_2)]^m\Delta\hat{Q}^{**m} \\ &\qquad = (\hat{L}_2\hat{L}_1^{-1})^m\Delta\hat{Q}^{*m} \\ &\text{Step 3} \quad \Delta\hat{Q}^m = (N^{-1}\hat{L}_2^{-1})^m\Delta\hat{Q}^{**m}\end{aligned} \quad (15)$$

where

$\Delta\hat{Q}^m = \hat{Q}^{m+1} - \hat{Q}^m$

$RHS^m = -(\hat{Q}^m - \hat{Q}^n) - \Delta t\{\hat{\mathcal{F}}^*(\hat{Q}^m) + \hat{\mathcal{F}}^*(\hat{Q}^n)\}/2$

m is the number of the Newton iteration. If $m = 0$, then $\hat{Q}^m = \hat{Q}^n$. And if $m \Rightarrow \infty$, then $\Delta\hat{Q}^m \Rightarrow 0$, that is $\hat{Q}^m \Rightarrow \hat{Q}^{n+1}$ and we can obtain a maximum second-order accuracy in time.

5. Numerical Results

As numerical examples, steady and unsteady transonic viscous flows around the NACA0012 airfoil at low and high angles of attack in the moist air are calculated.

5.1 Low angle of attack

The 2-D transonic flow around the NACA0012 airfoil at 2 deg. angle of attack is first calculated. Steady state solution is assumed. The computational grid used here is a standard C-type grid which has 201 × 83 grid points. The flow conditions are that the uniform Mach number, the stagnation pressure, the stagnation temperature and the Reynolds number (dry air) are specified as 0.75, 1.0×10^6[Pa], 293[K] and 6.0×10^6, respectively. As the relative humidity, 0%(dry air), 50%, 60%, and 70% are considered.

The calculated pressure coefficient distributions on the airfoil surface for the case of 0% humidity (ideal-gas, dry air) and the 70% humidity(two-phase flow) compared to the experiment of the dry air are shown in Fig.1. The result of the ideal-gas agrees very well with the experiment. However, the result of the two-phase flow is inconsistent with the experiment on the upper surface. It is explained that the lift loss is due to the occurrence of the condensation shock which is a typical phenomena formed when the growth of the droplet releases the latent heat.

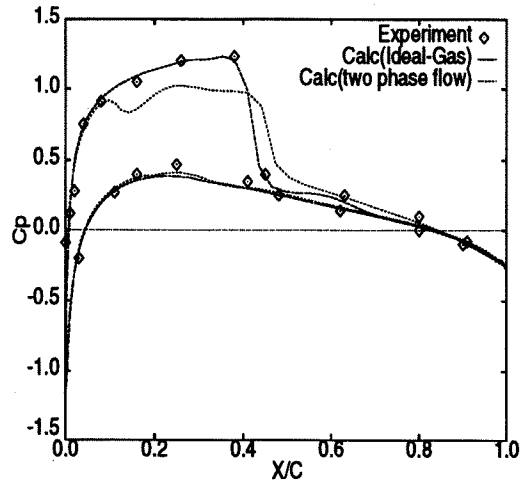

Fig.1 Pressure coefficient distributions on the airfoil surface

Figure 2(a)-(c) show the calculated contours of the Mach number, nucleation rate, and the condensate mass fraction, respectively. It is observed in Fig.2(a) that a condensation shock occurs near the leading edge of the airfoil as well as the normal shock at the mid of the airfoil. It is also explained using Figs.2(b) and 2(c) that the nucleation is started just from the leading edge and the droplets grow rapidly in the expansion region. The point at the rapid increment of the droplets is coincident with the point at the condensation shock. Therefore, it is verified that the reason of the condensation shock making is vary related to the release of the latent heat.

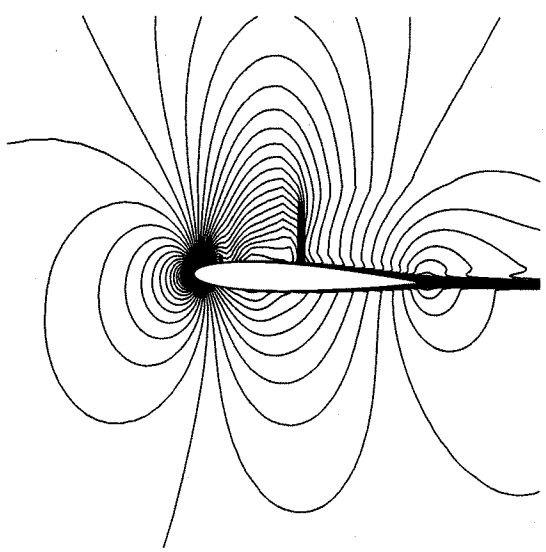

Fig.2(a) Mach number contours

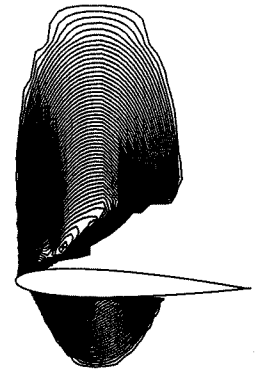

Fig.2(b) Nucleation rate contours

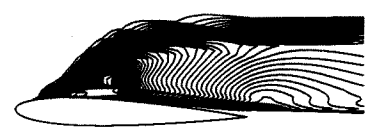

Fig.2(c) Condensation mass fraction contours

Figure 3 shows the lift/drag ratio plots obtained at the different relative humidities. Obviously, the ratio becomes worse according to the increment of the humidity.

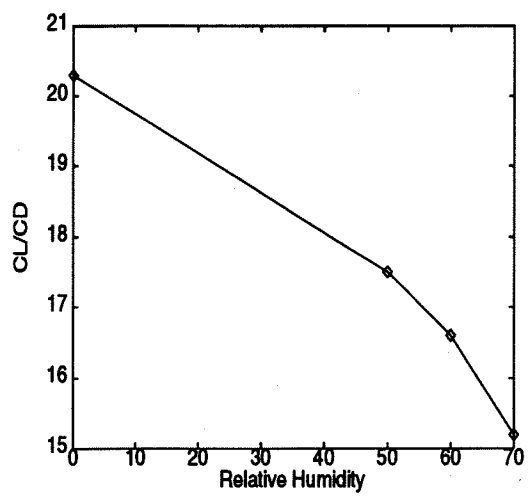

Fig.3 Lift/drag ratio distributions

5.2 High angle of attack

The unsteady 2-D transonic viscous flows around NACA0012 airfoil at 15 deg. angle of attack are next calculated. Figure 4 shows the computational

grid which forms the overset grid composed of a C-type grid around the airfoil(121×41 grid points) and a rectangular grid for the flow field(121×101 grid points). This grid system is used to obtain not only the accurate results near the airfoil but those far behind the body, especially those of vortex behavior. Variables are explicitly exchanged from each grid by the third-order Lagrange interpolation. As the flow conditions, the uniform flow Mach number is specified to 0.8. The case of the 0% humidity(ideal-gas, dry air) and the 60% humidity(two-phase flow) are considered. The other conditions are same with the previous low angle problem.

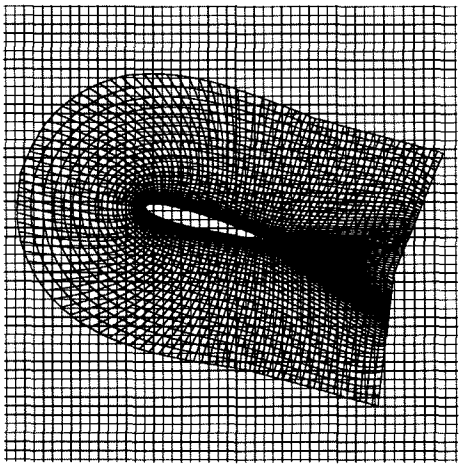

Fig.4 Schematic of the overset grid system

The calculated instantaneous Mach number contours and the vorticity contours for the ideal gas and the two-phase flow are shown in Figures 5(a)(b) and 6(a)(b), respectively.

In Figs.5(a) and 5(b), very clear periodical vortices are captured which are due to the interaction between the normal shock and the large separated boundary layer. On the other hand, although no clear condensation shock is found in Fig.6(a), the wake in Figs.6(a) and 6(b) is considerably disturbed and the flow region of the influence is more widely spread than the former case.

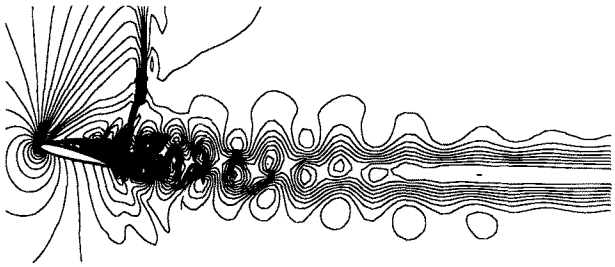

Fig.5(a) Instantaneous Mach number contours

Fig.5(b) Instantaneous vorticity contours

Fig.6(a) Instantaneous Mach number contours

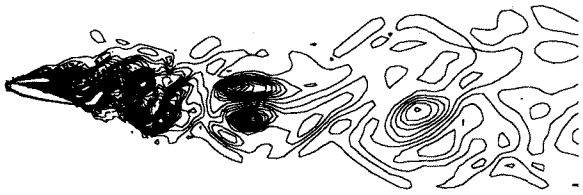

Fig.6(b) Instantaneous vorticity contours

Figure 7(a) and 7(b) show the contours of the calculated instantaneous nucleation rate at the different non-dimensional time. Also Figs.8(a) and 8(b) are the corresponding condensation mass fractions. Similar nucleation with the low angle case is observed on the upper side of the airfoil started from the leading edge. The interesting thing is that nucleations also appear at the discretized points in the unsteady wake. The location are coincident with the center of each strong vortex. The results in Figs.8(a) and 8(b) indicate that droplets generate near the airfoil and also additional droplets are produced in the wake region, and that both droplets are mixed and streaming downward. The boundaries of gas and liquid phases are clearly formed in the unsteady wake. Since the mass of liquid affects the wake, it must be considerably disturbed compared to the ideal-gas case. Another interesting phenomena observed is the occurrence of some hole shaped regions without the droplets in the wake.

Fig.7(a) Instantaneous nucleation rate contours

Fig.7(b) Instantaneous nucleation rate contours

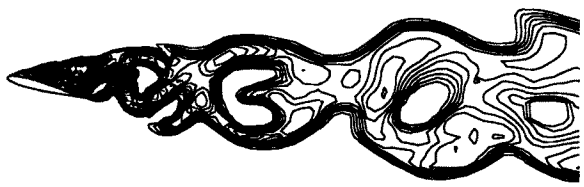

Fig.8(a) Instantaneous condensation mass fraction contours

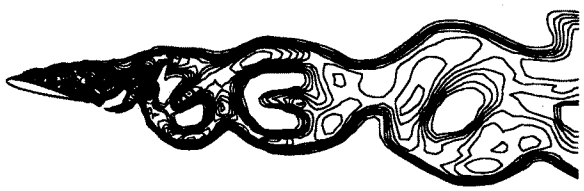

Fig.8(b) Instantaneous condensation mass fraction contours

6. Concluding Remarks

As strongly non-linear flow problems, unsteady transonic viscous flows around the NACA0012 airfoil in the moist air have been investigated using a higher-order accurate numerical method. The cases of the low and high angles of attack are calculated and the influence of the moist air to the performance of the airfoil is preliminary estimated. The results are summarized as follows.

1) the nucleation and the growth of the droplet could have been estimated using the present model equations based on the classical condensation theory.

2) the condensation shock due to the release of the latent heat has been clearly obtained in the case of the low angle of attack in the moist air.

3) the lift/drag ratio has become worst according to the increment of the relative humidity.

4) unsteady wakes influenced by the humidity have been obtained at the high angle of attack.

5) the wake has been considerably disturbed by the occurrence of the liquid phase.

6) nucleations and the condensation have been also observed in the wake.

7) the wake has had hole regions without droplets.

However, since the present method might be still preliminary one for estimating the condensation phenomena, further modifications should be necessary to obtain more accurate quantitative values

References

1. Pulliam T.H. and Steger, J.L., AIAA Paper 78-10.
2. Thomas, J.L. and Newsome, R.W., AIAA Paper 86-1049.
3. Steger, J.L., *AIAA J.*, Vol.16, 1978, pp.679-686.
4. Jameson, A., AIAA Paper 87-1184.
5. Harten, A., *J. Comp. Phys.*, Vol.**49**, 1983, pp.357-393.
6. Yee, H.C., *J.Comp.Phys.*, Vol.**68**, 1987, pp.151-179.
7. Ying, S.X., Schiff, L.B., and Steger, J.L, AIAA Paper 87-1207.
8. Risk, Y.M. and Gee, K., AIAA Paper 91-0020.
9. Yamamoto, S. and Daiguji, H., *Computers & Fluids*, Vol. **22**, 1993, pp.259-270.
10. Yamamoto, S., Takahashi, A. and Daiguji, H., AIAA Paper 94-2305.
11. Young, J.B., *Trans. ASME, J. Turbomachinery*, Vol.**114**, 1992, pp.569-579.
12. Schnerr, G.H., *Comp. & Fluids*, Vol.**22**, 1993, pp.103-116.
13. Ishizaka, K., Ikohagi, T. and Daiguji, H., *Proc. of 6th ISCFD*, Vol.**1**, 1995, pp.479-484.
14. Degani, D. and Schiff, L.B., *J.Comp.Phys.*, Vol.**66**, 1986, pp.173-196.
15. Frankel, J., "Kinetic Theory of Liquids," 1955, Dover.
16. Young, J.B., *Trans. ASME, J. Engineering for Gas Turbines and Power*, Vol.**110**, 1990, pp.1-7.
17. Schnerr, G.H. and Dohrmann, U., *AIAA J.*, Vol.**28**, 1990, pp.1187-1193.
18. Anderson, W.K., Thomas, L. and van Leer, B., *AIAA J.*, Vol.**24**, 1986, pp.1453-1459.
19. Harten, A., *J. Comp. Phys.*, Vol.**83**, 1989, pp.148-184.
20. Steger, J.L. and Warming, R.F., *J. Comp. Phys.*, Vol.**40**, 1981, pp.263-293.
21. Roe, P.L., *J. Comp. Phys.*, Vol.43, 1981, pp.357-372.